actuators

MDPI

Article

Design and Testing of a Hollow Continuum Magnetic Millirobot with Multimodal Motion

Yuanhe Chen †, Zichen Xu † and Qingsong Xu *

Department of Electromechanical Engineering, Faculty of Science and Technology, University of Macau, Avenida da Universidade, Taipa 999078, Macau, China
* Correspondence: qsxu@um.edu.mo
† These authors contributed equally to this work.

Abstract: Magnetic continuum millirobots have presented outstanding potential in ultrahigh-precision engineering including minimally invasive surgery, due to their flexible mechanical structures and dexterous manipulation. Traditional continuum millirobots exhibit limited cargo-loading capacity, which restricts their application. Herein, we propose a novel design scheme of a magnetically actuated untethered hollow continuum millirobot. The millirobot is composed of silicone as the mainframe structure and two tiny magnets for actuation. To improve the loading capacity, partial silicone is removed to create a flexible cavity, which enables cargo delivery and potential in vivo sampling functions under wireless magnetic actuation. Theoretical analysis and experimental testing are conducted to reveal the effectiveness of the proposed design. The soft structure brings a new strategy to achieve multimodal motion including rolling, tumbling, and swinging. Moreover, the magnet part can generate a powerful magnetic force output for dexterous manipulation. These functionalities lay a foundation for playing a greater role in next-generation biomedical applications.

Keywords: microrobotics; magnetic actuation; continuum millirobot; untethered soft robot; mechanism design

Citation: Chen, Y.; Xu, Z.; Xu, Q. Design and Testing of a Hollow Continuum Magnetic Millirobot with Multimodal Motion. *Actuators* **2022**, *11*, 269. https://doi.org/10.3390/act11100269

Academic Editors: Takeshi Mizuno and Steve Davis

Received: 3 July 2022
Accepted: 14 September 2022
Published: 20 September 2022

1. Introduction

Mobile microrobots have demonstrated attractive performance in various assignments at a small scale, especially in medical applications. The mini-level physical size of microrobots enables more precise operations in crowded and extreme environments. It facilitates reaching deeper tissues within the human body, where untethered actuation mechanisms [1,2] play a profound role. With the help of recent development and breakthrough in material [1,3], chemistry [4], and biotechnology [5], plenty of microrobots have been designed and put into concrete experimental applications, including actuation [6–8], navigation [9], control [10], and execution [1]. However, it remains a challenge to further promote microrobots' functionalities for more practical applications.

Among recent works, increasing attention has been focused on detailed clinical scenarios, such as cardiovascular diseases, which cause numerous death all over the world [11–13]. To overcome the current medical equipment's limitations in invasive surgeries, catheter-based continuum microrobots have been developed [1,14,15] to intrude into hard-to-reach corners, where the controlled magnetic fields contribute to high-efficiency untethered actuation. These works have revealed the attractive advantages of continuum structures, especially in endovascular surgeries. Nevertheless, from the perspective of functionalities and designs, relatively simple mechanical structures cannot enable more potential usage schemes. For example, polydimethylsiloxane (PDMS) was utilized to connect two permanent magnets, by which the continuum microrobot was produced for flexible magnetic actuation [16]. The solid continuum structure and complex structural design limits the diversity of applications [7,17–20], such as cargo loading, which is significant to achieve live sampling in deeper tissues, in view of the sampling procedure in the medical scenarios.

Proper mechanical design improvement and size optimization [2] is a potential solution for strengthening such functionalities.

Herein, we propose a novel design scheme for an untethered multifunctional hollow continuum magnetic millirobot (MHCMM). The MHCMM is constructed by integrating silicone as the main frame structure and several miniaturized magnets for actuation. The removal of some non-magnetic connecting parts in the millirobot creates a flexible cavity, which improves the cargo-loading capacity and enables cargo delivery during a potential bio-sampling role under a wireless magnetic drive. It is notable that the operating space of the MHCMM is limited to microscopic scales, such as multimodal motion range within 0.5 mm in each axis and a sampling capacity of 300–600 µL, which is beneficial for future exploration tasks in vivo. By controlling the external magnetic field, the MHCMM can offer multimodal motion and execute dexterous manipulation. In addition, the MHCMM is capable of producing an output force of 5–15 mN, which enables it to exert a sufficient force on the objects such as tumors in the human body. With the help of a magnetic navigation system powered by permanent magnets mounted on a robot arm, the wirelessly actuated millirobot is promising for minimally invasive surgery. It facilitates more flexible motion, where two-dimensional electromagnetic coils serve as the local actuation device. The reported multifunctional hollow continuum magnetic millirobot demonstrates great potential for minimally invasive surgery.

Compared with existing works [2,7,8], the novelty of the proposed MHCMM lies in the simplified sampling method, risk reduction of drug leakage, and more functions such as cargo transportation and output force test. The remaining parts of the paper are organized as follows. The design and modeling of the magnetic millirobot are presented in Section 2. The prototype fabrication and experimental investigations are outlined in Section 3, where the experimental results are given and the discussion is addressed. Section 4 concludes this paper.

2. Design and Modeling

2.1. Design Scheme

At small scales, it is important to support more functionalities by microdevices in a constrained space. For continuum millirobots, previous work utilized various soft materials to construct solid structures, which serve as the connecting parts or main structure of the millirobots [20,21]. Such a design achieved outstanding deformation and control results. However, the fully solid structures cause some wasted space, which is designed to integrate other functionalities. Here, we transform the soft structure into a hollow one. The redundant parts are supposed to be removed, which results in a novel hollow millirobot. As shown in Figure 1a, this design provides more usable space for cargo loading and sampling.

To form a cavity structure, we used rapid-forming silicone over the top of a thin glass tube (outer diameter of 0.5 mm) to allow it to settle naturally. In addition, we can control the magnetism at the end of the magnets (at both ends) to perform different functions. By tuning the distribution of the poles at both ends of the MHCMM, a circle structure and an arch structure can be obtained, respectively, as shown in Figure 1b. Under the steering of external magnetic fields, this concept design brought a new solution to the mechanical design of soft millirobots.

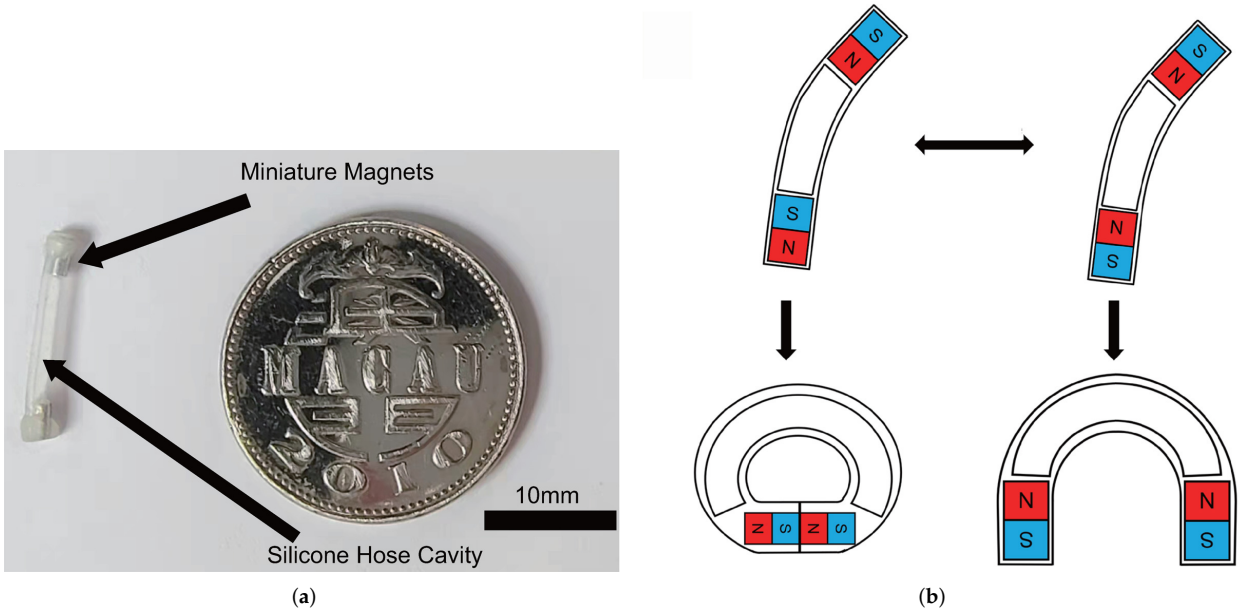

Figure 1. Physical prototype and illustration of the working principle of the MHCMM. (**a**) The main structure of the MHCMM is composed of two miniature magnets at the two terminals and a silicone hose cavity in the middle. (**b**) The magnetism at the end of two magnets can be controlled to perform different functions. When the poles at both ends of the MHCMM are tuned to be the same polarity, an arch shape can be produced by applying an external gradient magnetic field. When they have different polarity magnetic poles, a circumferential shape can be generated.

2.2. Physical Modeling

2.2.1. Magnetic Actuation

The introduction of magnetic parts plays a significant role in actuating and controlling the millirobot. For realizing magnetic field actuation, we consider an axially magnetized cylindrical NdFeB (N52-grade) magnet with an axial-symmetric magnetic field distribution. The magnet has a radius of R and a length of 2R. For the permanent magnet with the same diameter and length, the distribution of the magnetic field remains constant when the characteristic dimensions of the magnetized body are normalized [15,22,23]. Thus, we can express the magnetic field at a determined spatial location in the form of a normalized vector function as follows:

$$\mathbf{B}(\mathbf{p}) = B_m \mathcal{F}(\mathbf{p}/R) \tag{1}$$

where $\mathbf{p}$ denotes the position vector with respect to the center of the magnet in cylindrical coordinates, B_m is the remanent magnetization of the magnet, and $\mathcal{F}$ represents the vector function (its implicit form is given in [24–26]).

Along the central axis of the magnet, we can explicitly express the magnitude of the magnetic field in the normalized form below:

$$B = \frac{B_m}{2}\left(\frac{d/R+1}{\sqrt{(d/R+1)^2+1}} - \frac{d/R-1}{\sqrt{(d/R+1)^2+1}}\right) \tag{2}$$

where d is the distance from the center of mass of the permanent magnet to the measurement point along the centerline.

From Equation (2), we can see that the magnetic field strength decreases as the normalized distance d/R increases. Thus, a large-enough external magnet is required to impose an actuation effect to guide the MHCMM within a reasonable working distance. Generally, the task of controlling the MHCMM requires a maximal magnetic field strength of 20–40 mT. Then, d/R = 0.66–1.34 can be derived according to Equation (2). Thus, we can calculate the required external magnet, i.e., a cylindrical permanent magnet with a diameter and length

of 300 mm (with R = 150 mm) and B_m= 0.574 T. The normalized distance is translated into a distance, which is at least 284 mm from the center of the magnet (or 134 mm from the surface of the magnet).

In principle, a magnetized object in a magnetic field suffers from a magnetic force and a magnetic torque. The equations for the magnetic force and magnetic torque of an object subjected to magnetization in a magnetic field are both related to the gradient of the magnetic field, as follows:

$$\tau_m = \int_{V_m} \mathbf{M} \times \mathbf{B} dV_m \tag{3}$$

$$\mathbf{F}_m = \int_{V_m} (\mathbf{M} \cdot \nabla)\mathbf{B} dV_m \tag{4}$$

where **M** is the magnetization of the object and V_m is the volume of the magnetized object. All of these magnetic interactions determine the effects of magnetic actuation.

2.2.2. Robot Deformation

When manipulating the MHCMM with different polarities at both ends, the S-pole of the permanent magnet is initially placed in the positive Z-axis direction. This causes the MHCMM to remain standing at one end, along with an inclined angle for the other end. Ideally, the MHCMM should be purely vertical if the external permanent magnets are placed in the given position. In practice, the silicone material does not exhibit a uniform density, resulting in a slight bending deformation. This state is the result of several forces interacting together, such as the attractive force of opposite-pole magnets F_{M1}, repulsive force of same-pole magnets F_{M2}, and supporting force of materials F_{e1}, as shown in Figure 2A.

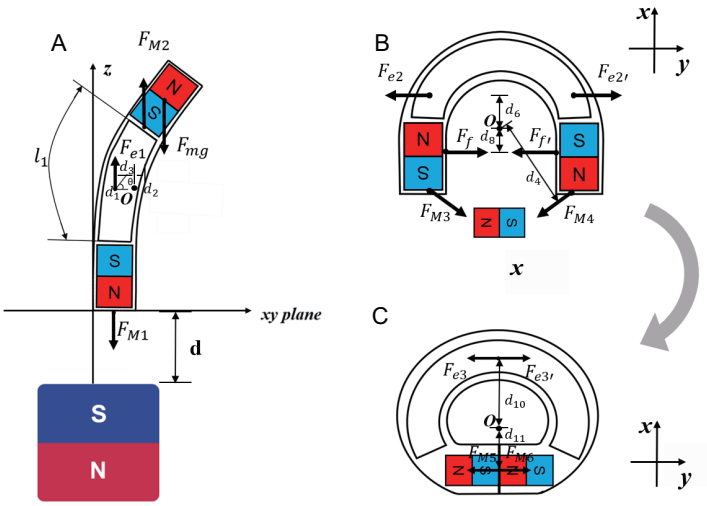

Figure 2. Physical analysis of MHCMM in three force states (lateral view). (**A**) Standing at one end; (**B**) leading the attraction process at both ends; (**C**) knotting into a circle.

Its static deformation is described by a linear elastic strain model, which is given by:

$$F_{e1} = \frac{E_1 dLS}{L} \tag{5}$$

where S is the maximum cross-sectional area of the MHCMM cavity, E_1 is the Young's modulus, and dL/L is the elongation of the cavity divided by the original length.

Through the above equation, the bearing force of the cavity F_{e1} is analyzed below.

$$0 = F_{M1} \cdot d_1 + F_{M2} \cdot d_2 + F_{e1} \cdot d_3 \tag{6}$$

where F_{M1} and F_{M2} are the forces applied to the magnets at both ends. d_1, d_2, and d_3 are the distances from the point of force to the center of mass of the cavity. Their sum is 0, which ensures a stable standing condition for the MHCMM.

Referring to Figure 2B, we use a small magnet to attract both ends of the MHCMM (with double-ended anisotropic poles) to contact each other in a plane. Due to the friction force and suction force of the anisotropic poles canceling each other, the elastic tension of silica gel is derived as follows:

$$0 = F_{M3} \cdot d_4 + F_{M4} \cdot d_5 + F_{e2} \cdot d_6 + F_{e2'} \cdot d_7 + F_f \cdot d_8 + F_f \cdot d_9 \quad (7)$$

where F_M is the shaped magnet attraction, F_f is the friction between the MHCMM and the plane, and F_e is the elastic tension of silica gel. In this way, MHCMM will form the shape as shown in Figure 2B. Subsequently, we remove the external small magnet, and the magnetic poles at both ends of MHCMM will attract each other to form a circle, as shown in Figure 2C.

3. Prototype Fabrication and Experimental Results

3.1. Prototype Fabrication and Experimental Setup

3.1.1. Material and Fabrication

For the potential clinical application of this millirobot, we selected several types of fabrication materials by considering biocompatibility, optimal working temperature, and other factors. In particular, five different soft materials (i.e., Dragon Skin 10 Medium (from Smooth-on Inc., East Texas, PA, USA), Dragon Skin 30 (from Smooth-on Inc.), Finished Silicone (from Runze Fluid Co. Ltd., Nanjing, China), E610 (from Hongye Technology Co. Ltd., Shenzhen, China), and E630 (from Hongye Technology Co. Ltd.)) are adopted as candidates to assemble the MHCMMs (e.g., making thin tubes out of silicone inverted molds). The cavities are created by heating and solidifying after natural dropping on a thin glass tube with a radius of 0.3 mm.

Due to the material property, only three of the five materials can be used to produce the prototype of the MHCMM. The adopted materials and their properties are shown in Table 1. The other two materials (E610 and E630) are not feasible because they are too viscous, which has a negative impact on forming cavities. For each of the three MHCMM samples, after fabricating the MHCMM sample with a length of 20 mm, it was stretched by increasing the distance between two magnets at the terminals. The original and maximally deformed lengths were measured for each stretch. The experiment was repeated six times, and the experimental results are shown in Figure 3. We can observe that the silicone material of Dragon Skin 10 Medium provides the best tensile property, which is stretched about 1.55 times on average.

We used rapid-forming silicone over the top of a thin glass tube (outer diameter: 0.5 mm) to allow it to settle naturally to form a cavity structure. Furthermore, its effective working temperature (−65 °F to 450 °F) also meets the requirements of our working environment (i.e., 99.5 °F, the internal ambient temperature of humans). Thus, the prototype with this material is chosen for the subsequent tests.

Table 1. Millirobot materials and properties.

Material Name	Material Properties	Stretching Rate
Dragon Skin 10 Medium	Shore hardness: 10A, Specific gravity 1.07 g/mL, Tensile strength: 475 psi	1.55
Dragon Skin 30	Shore hardness: 30A, Specific gravity 1.08 g/mL, Tensile strength: 500 psi	1.34
Finished Silicone Tube	Rockwell hardness: 70A	1.42

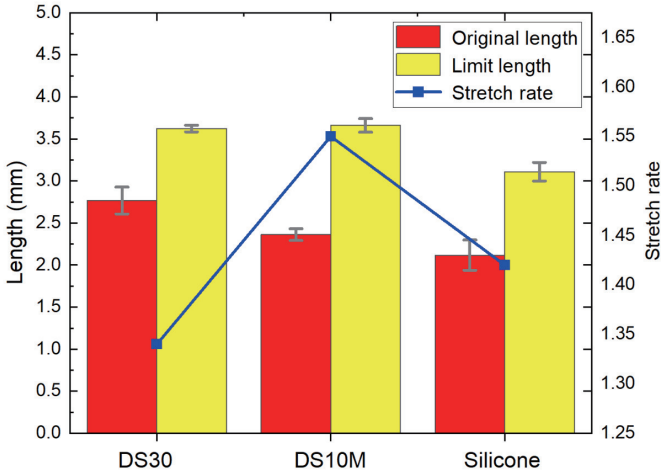

Figure 3. Test results of three types of materials. In the histogram, error bars compare the properties before and after stretching.

3.1.2. Experimental Setup

For the experimental study, we adopted a magnetic driving system that consists of a three-axis orthogonal electromagnetic coil device, a tube vessel (35 mm diameter) containing the millirobot, a top camera, and a side movable camera, as shown in Figure 4. A triaxial electromagnetic-coil actuation system generates the oscillating magnetic field, with each of the three orthogonally arranged coils driven by a servo amplifier (KXN-6020D DC, from Zhaoxin Inc., Shanghai, China). The amplifier was controlled via a digital I/O board by a developed LabVIEW program (National Instrument Inc., Pinehurst, NC, USA) running on a personal computer.

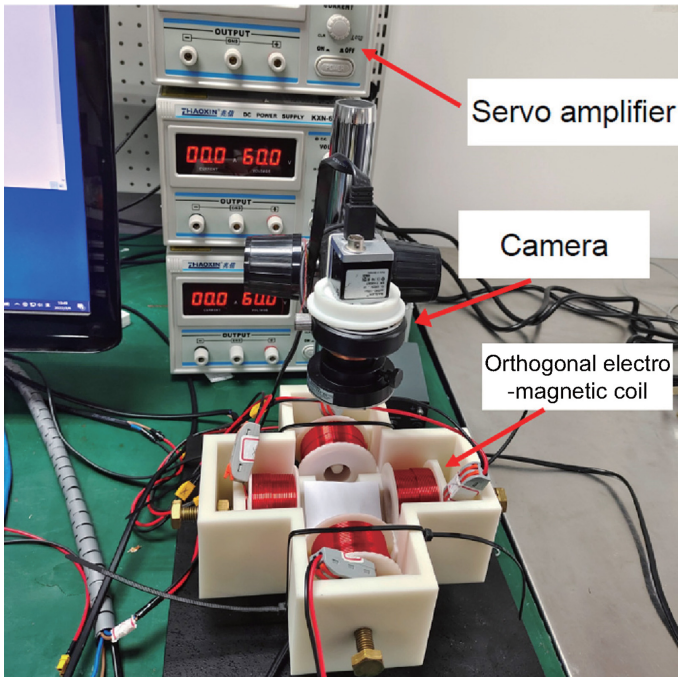

Figure 4. Experimental setup of a magnetic actuation system consisting of a three-axis orthogonal electromagnetic coil device, a Petri dishes (35 mm in diameter) with the robot inside, a top camera, and a side movable camera.

3.1.3. MHCMM Characterization

Since understanding the support capability of the MHCMM's inner cavity structure is the basis for the next step in the control of its unidirectional oscillation, it is necessary to

measure the bending angle of the MHCMM under different magnetic field strengths. Here, we fixed one end of the MHCMM, and then applied different currents to the electromagnetic coil on the Z-axis of the MHCMM as shown in Figure 5A. The experimental test diagram and results are shown in Figure 5B.

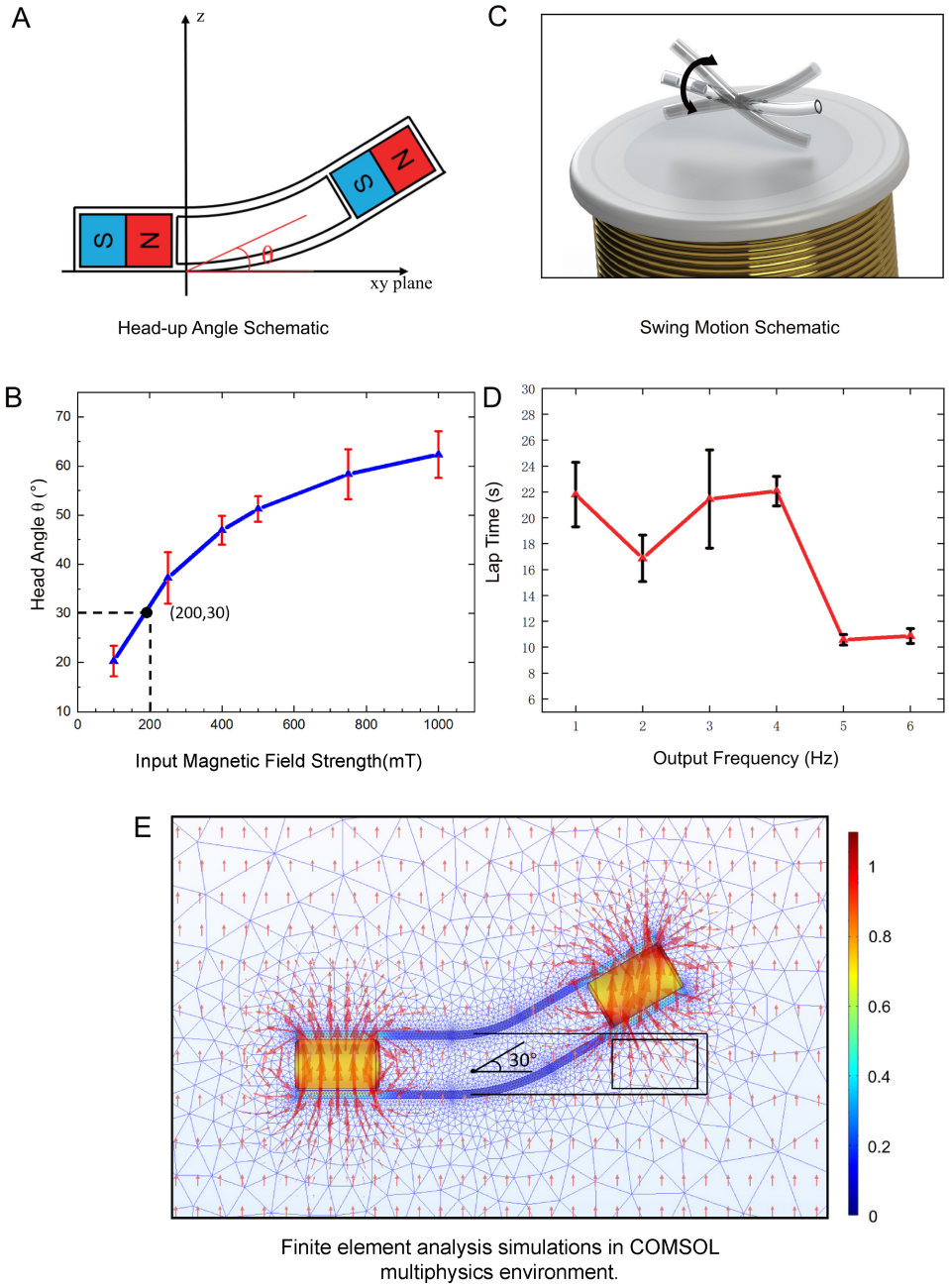

Figure 5. Head-up test and swing motion results. (**A**) The head-up angle of the MHCMM itself can be obtained by changing the input signal to the electromagnetic coil amplifier. (**B**) Experimental results of six sets of head-up angles versus input magnetic field strength. (**C**) A 3D schematic of oscillating forward motion with an electromagnetic coil underneath, which produces an oscillating magnetic field. (**D**) The electromagnetic coil, which has an output magnetic field strength of 300 mt, is controlled to produce an oscillating magnetic field of different frequencies, and the lap time is the time taken to make one revolution along a 35 mm diameter Petri dish. (**E**) The deformation of MHCMM under the action of an external magnetic field of strength 210 mT. The analysis result is consistent with the test result.

3.2. Experimental Results

3.2.1. Navigation Control Results

After fabricating the MHCMM, we installed permanent magnets at the end of a robot arm (R14000 dual-arm robot, from ABB Ltd., Zürich, Switzerland) with custom-built parts (THREE-M 3D printer, from Wiiboox.net Inc., Nanjing, China). A model structure of human blood vessels was built and manufactured using transparent resin by 3D printing. The main parts of the aorta, renal artery, common skeletal artery, and superior mesenteric artery are involved in the 3D vascular model. In consideration of the plasma density of the human body [27], an aqueous solution of 30% glycerol was chosen for filling the 3D vascular model in the experimental study.

The robot arm is programmed to guide the MHCMM to move along a predefined motion trajectory in the vascular pipeline for arriving at the target point. Due to the multidimensional motion of the robot arm, we not only can program the motion trajectory in the two-dimensional plane but also can set the motion program in three dimensions. Based on the previously calculated attraction force between the permanent magnet of the robot arm and the miniature magnetic robot, we found that the robot arm can carry the end-effector magnet well, and thus guide the MHCMM to deliver the catheter inside the 3D vascular model, as shown in Figure 6.

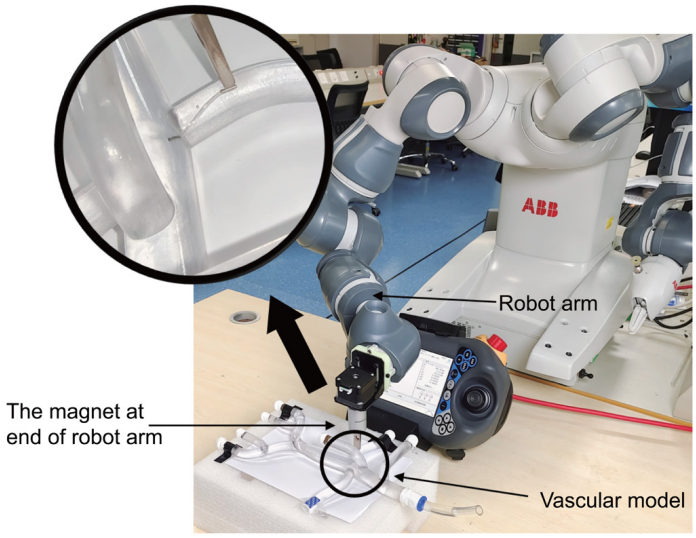

Figure 6. The MHCMM is moved to the perimeter of the target position by a permanent magnet fixed at the end of a robot arm.

Considering the limitation of precision, the robot arm cannot guarantee local precise navigation control. Hence, a coarse-fine strategy is adopted to improve the precision by the combination of a robot arm and an electromagnetic coil system. After a long-trip navigation by the robot arm, the electromagnetic coil system serves as a subsequent actuation device for more precise local navigation. We used an oscillating magnetic field to drive the MHCMM for swing motion, as shown in Figure 5C. The MHCMM produces turbulence at frequencies above 7 Hz. Thus, its performance is measured at frequencies from 1 to 6 Hz. The MHCMM has the best frequency response at 5 Hz, and it can go around the Petri dish in a shorter time with satisfactory stability.

To further demonstrate the advantages of the MHCMM in multimodal motion, we manipulate the external permanent magnet by hand to actuate the MHCMM. Both the circle structure and arch structure of MHCMM can tumble to the assigned target point, as shown in Figure 7A,B. Additionally, the tumbling motion of the MHCMM successfully crossed some obstacles, proving the ability to cross obstacles as shown in Figure 7C. Motion mechanics analysis of tumbling motion is shown in Figure 8. In addition, we explored a

worm-like motion of the MHCMM, as shown in Figure 9. Due to this motion being mainly pulled by magnetic fields, it does not become a full-fledged motion, as shown in Figure 9.

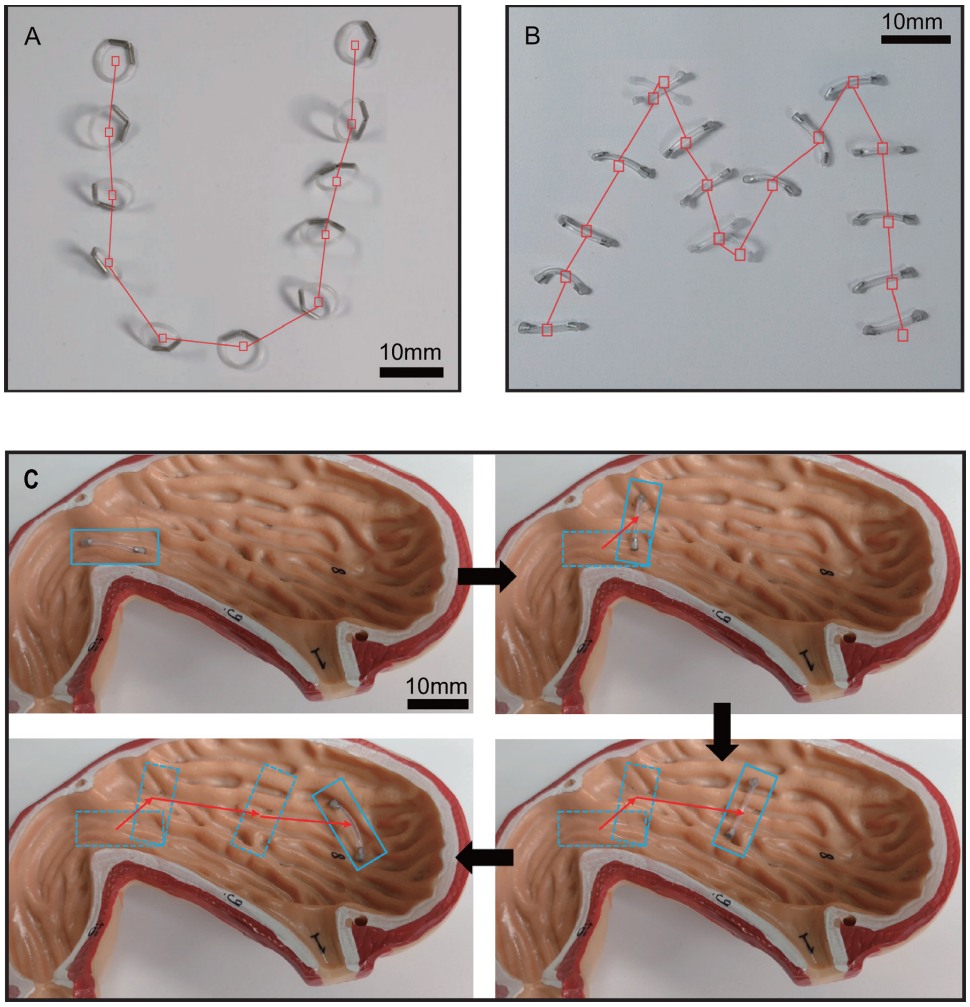

Figure 7. The multimodal motion of MHCMM. (**A**) The "U"-shaped trajectory by circular tumbling; (**B**) the "M"-shaped trajectory by the tumbling motion; (**C**) the MHCMM demonstrated the ability of the tumbling motion to cross obstacles by crawling by path in a human stomach model.

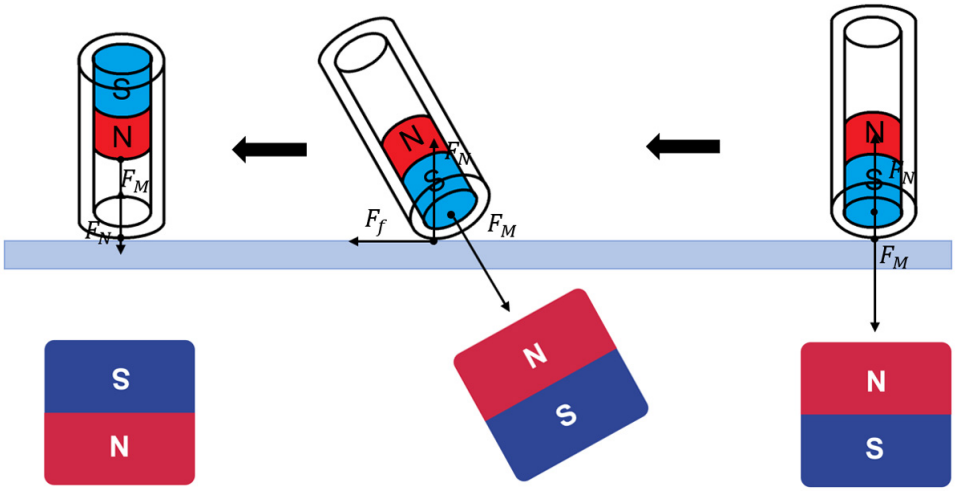

Figure 8. Motion mechanics analysis of tumbling motion. Different morphological forces are experienced when the MHCMM undergoes tumbling motion in the side view perspective.

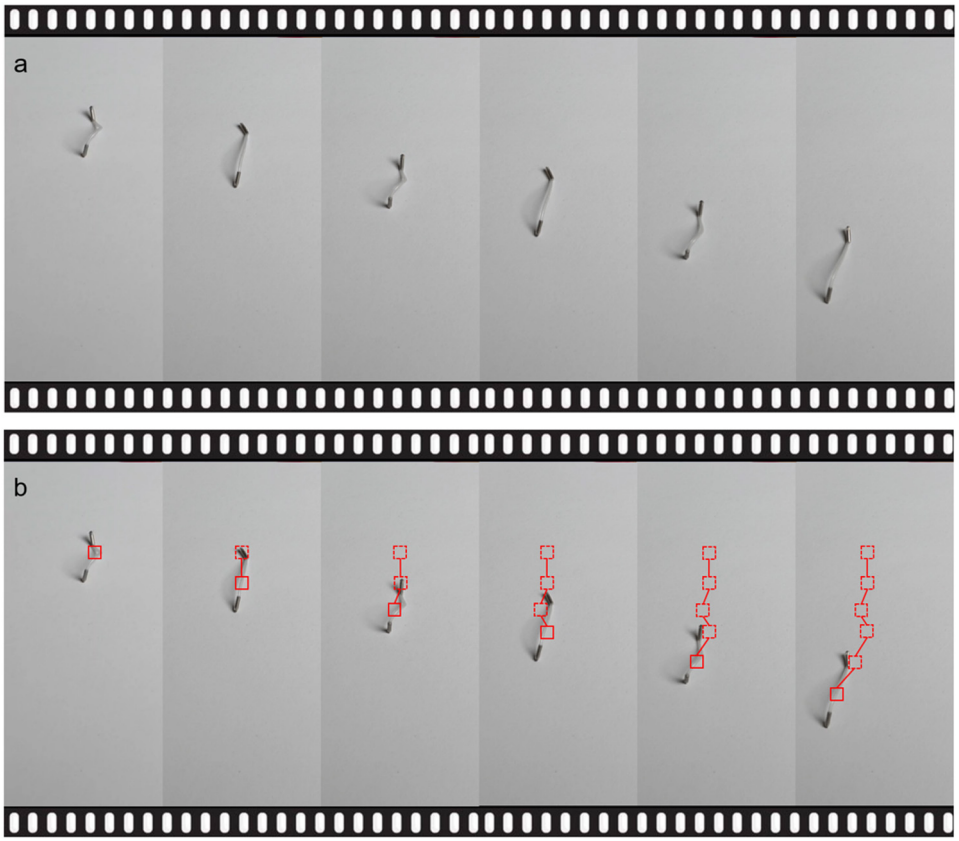

Figure 9. The worm-like motion and path of MHCMM. (**a**) By changing the distance of the external permanent magnet, the MHCMM with opposite magnet polarity at the end can perform a worm-like motion. (**b**) The path of worm-like motion of the MHCMM is marked.

3.2.2. MHCMM Function Test Results

The soft hollow structure design enables various potential medical applications. To test the functions of the MHCMM in drug delivery, material sampling, stirring, and manipulation, a series of experiments were conducted as follows.

The cavity of the MHCMM makes it accessible to load more cargo, which provides a tool for in vivo biological sampling and drug delivery. To demonstrate this functionality, stretch sampling was performed. In particular, the magnets at both ends of the MHCMM were tugged by the permanent magnets in hand for executing the outward stretching motion. In this way, the volume of the internal cavity of the MHCMM was increased, leading to filling in the cavity with external ambient fluid. After the external ambient fluid is mixed with the preservation fluid in the cavity, the external magnetic field is removed, and the MHCMM retracts. We repeated this operation several times to ensure the presence of external ambient solution in the MHCMM cavity. The final measurement can reach 300–600 uL of liquid volume per sample, which completely encompasses the requirements of biological sampling for the number of cells. The scheme of the biological sampling process is presented in Figure 10. What is more, the MHCMM uses a sample sampling port similar to the principle of a heart valve manufactured by needle hole injection, and the external pressure will effectively reduce its loss of internal cargo. In addition, if the MHCMM is loaded with drugs, we can also achieve targeted drug transport through the liquid exchange in the cavity.

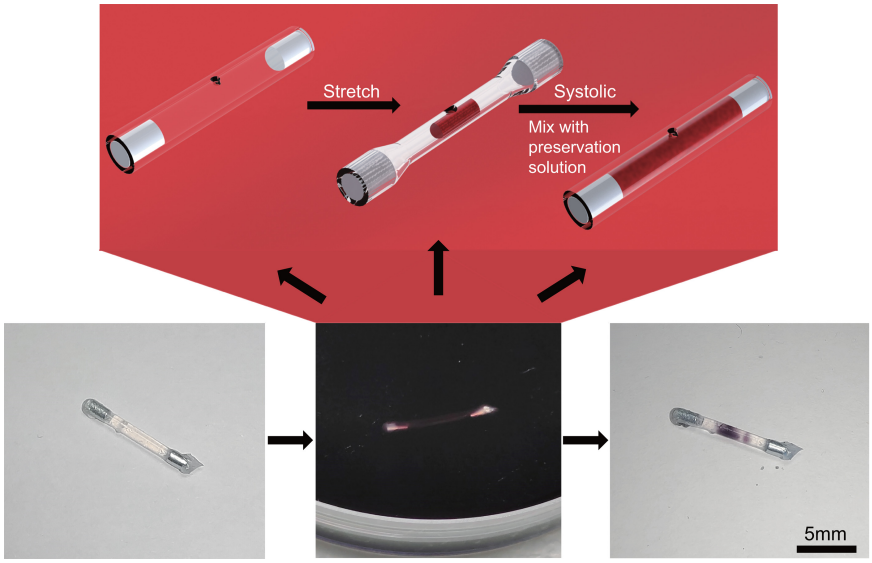

Figure 10. Illustration of material sampling by the millirobot. The MHCMM cavity was filled with water and then put into a colored solution for sampling testing.

For testing the stirring function of MHCMM, we regulated the external permanent magnet by hand to form a rotating permanent magnetic field. The experiment was conducted by using a double-ended anisotropic magnet MHCMM. According to a preliminary experiment, a double-ended magnet with a different polarity MHCMM easily forms an upright shape, which is suitable for stirring, as shown in Figure 11. We performed finite element analysis simulation by COMSOL software. The results demonstrate that with the same motion velocity, the string structure contributes more to the induced flow field, as shown in Figure 12. Whereas a double-ended magnet with the same polarity as MHCMM will exhibit an arch-like shape under the attraction of an external permanent magnet, which affects the stirring function. Driven by an external magnetic field, the MHCMM exhibits the function of stirring in water. According to this function, we can make the drug diffuse faster in the human body.

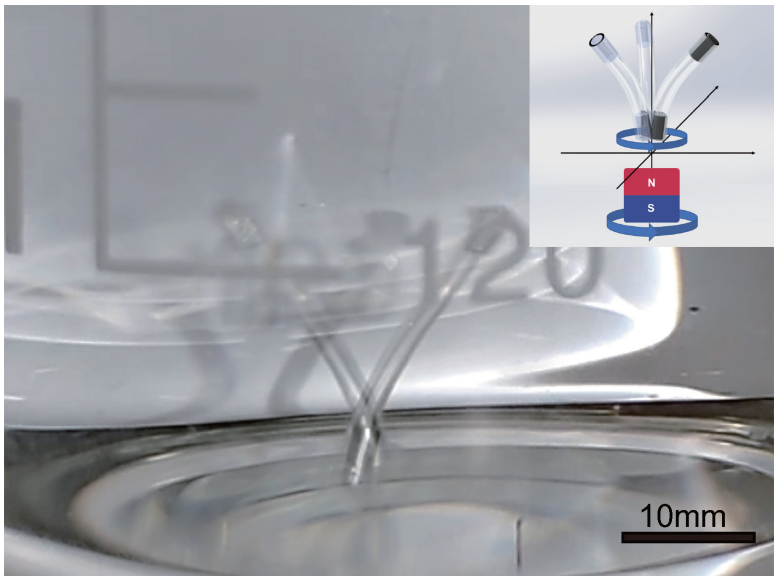

Figure 11. Stirring mode and physical demonstration. The MHCMM has the function of stirring in water, which is driven by the external magnetic field.

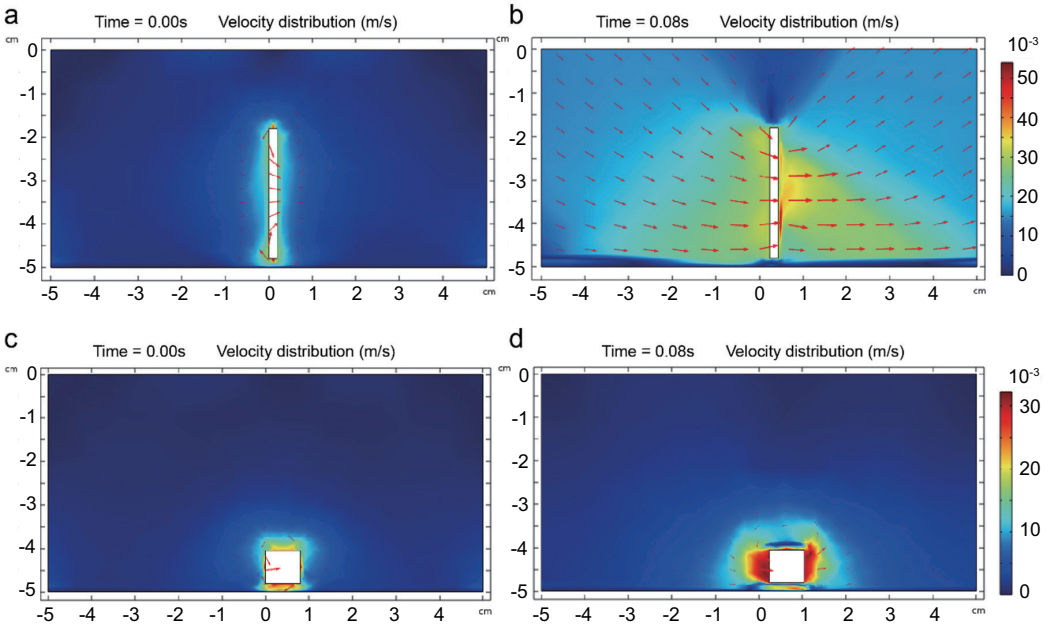

Figure 12. Simulation results of flow induction by the MHCMM. (**a**) The initial state (at 0 s) of the millirobot with the string structure is denoted by the slender square. (**b**) At 0.08 s, the slender square moves with a velocity of 3.0 cm/s. In the simulation, the total areas of the slender square and the flat square are identical. (**c**) The initial state (at 0 s) of the millirobot with normal structures, which are denoted by flat squares. (**d**) At 0.08 s, the squares move with a velocity of 3.0 cm/s.

Figure 13A shows the experimental setup for measuring the tensile force. In view of the potential of the circle-structure MHCMM for robotic manipulation, we accomplished target capture and measured its output forces, as shown in Figure 14. The experimental setup includes a microforce sensor (model 308445, from Zero Draft Inc.), which is an extended measurement range (extended force sensing range with a thin glass tube). One circle-structure MHCMM can manipulate the objects, as shown in Figure 13B. Its force signal is given in Figure 14a. This provides the experimental basis for the next step of MHCMM micromanipulation (e.g., pulling and snapping) of tumors in the vasculature.

From the experimental results, we found that two MHCMMs can form a bigger circle for executing the capture task of a larger target. Its output force signal is given in Figure 14b. Moreover, it is seen that the output force of the ring formed by the connection of two MHCMMs is greater than that of a single ring, which provides the indication for the next step of study in cluster control.

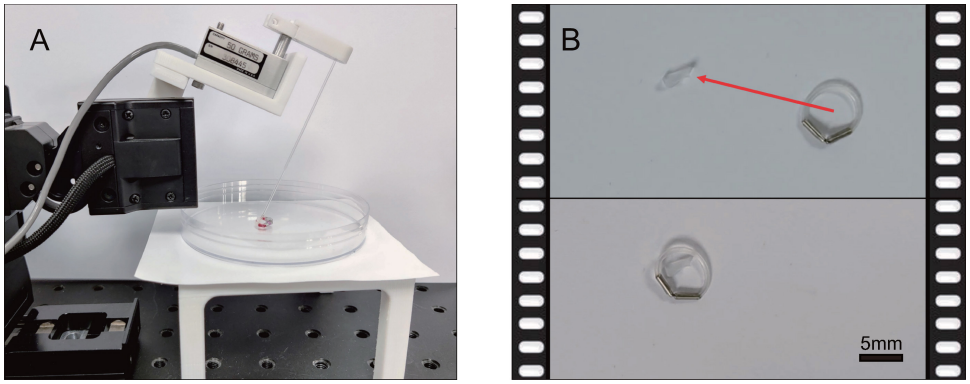

Figure 13. Illustration of re-configurable function and microforce measurement of a circular MHCMM. (**A**) Experimental setup of microforce measurement; (**B**) once the robot reaches the specified position, the hypothetical tumor (heteromorph) nesting is completed.

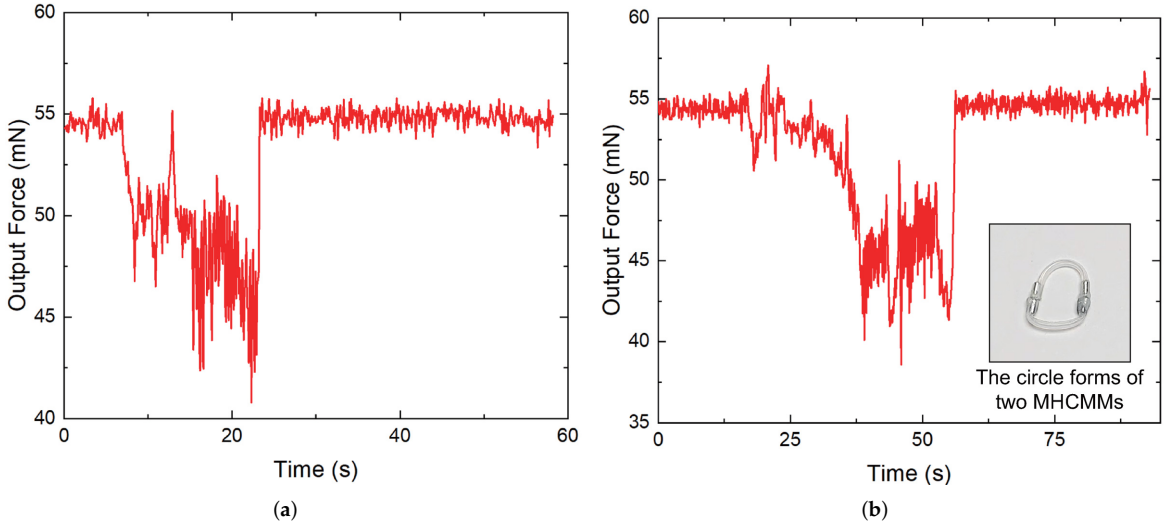

Figure 14. Microforce measurement result of circular MHCMM. (**a**) One ring is measured with the microforce measurement instrument for determining the tensile force, which can be released under constant magnetic field traction; (**b**) microforce measurement results with two MHCMMs, which provides an indication for the next step study of cluster control.

3.3. Discussion

We introduced a hollow mechanical structure to endow the ability to carry more cargo or potential functional components. Small permanent magnets can be easily actuated under various external magnetic fields, which brings diverse manipulation schemes for potential applications. Similar designs can be found in the literature [28], whose string-like mechanical structure is composed of a central magnetic beam with two identical buoyant components attached to its free ends. Its key actuation part is the magnetic beam between the two ends. With the help of the harmonic magnetization profile of the beam with a phase shift angle, six-degrees-of-freedom multimodal locomotion was obtained. However, the mechanical structure cannot provide available space for cargo loading. To solve this problem, in the literature [29], a magnetic soft capsule was introduced to overcome the disadvantage in cargo delivery. In addition, its robot footpad design brings more intriguing strategies in 3D locomotion. However, the introduced capsules increase the physical size, and environmental sampling remains a challenge. Compared with these works, our hollow mechanical design is more practical during long-trip navigation, guaranteeing the completeness of desired cargos.

In the literature, previous works have conducted fine attempts at hollow structure design for magnetic microrobots [2,7,8]. As compared with the endoscopic robot in the reference [2], the novelty of our proposed MHCMM lies in the optimized size of the robot and simplified sampling method for bio-liquids. As compared with the magnetic microrobot in [8], the novelty of the proposed MHCMM is the risk reduction of drug leakage. Unlike the sample output and input ports of the previous magnetic microrobot, our MHCMM introduces a simple sampling port, which is similar to the principle of a heart valve. The external pressure will effectively reduce the risk of internal cargo loss. In addition, as compared with the magnetic microrobot in [7], our proposed MHCMM has more practical functions, such as cargo transportation and output force test.

For many current continuum microrobots [15,16,21], there is still plenty of accessible improvement in their mechanical design, which should be paid more attention to remove unnecessary parts of the continuum millirobots to obtain more available space. In fact, the experimental results given in this paper indicate that the proper removal of solid structures has not severely reduced the functionalities of continuum millirobots. The increment of space is essential for further promoting the continuum millirobot, and the decrease in volume size reduces the potential dangers of blockages in vessels. The hollow

design allows more space for integrating other necessary components, such as sensors and other components. For live sampling tasks, this design helps to reach deep tissues within the human internal body and carry more medical material for potential treatments. However, this promotion is limited because the long and hollow continuum part lacks sufficient rigidity, leading to poor performance in robotic manipulation tasks. More research will be conducted to reveal the optimal distribution of the hollow parts as well as the small permanent magnets in future work. It is also a big challenge to realize the precise control of sampling and releasing tasks, which is significant for safety and efficiency in medical scenarios. Moreover, free from the guidewire, the untethered millirobot can demonstrate more personalized operations, such as tumbling and deformation functions. Such untethered designs reveal potential research in multiple millirobot system control, which is a promising solution for further promoting the performance of millirobot systems in future work.

4. Conclusions

In this paper, we proposed a new soft continuum millirobot design promoting the functionalities and locomotion flexibility for potential intravascular applications. This millirobot is composed of two parts: (1) two small permanent magnets at the two ends, enabling powerful actuation for getting rid of the reliance on guidewire-based equipment; (2) soft materials as the combination part for the two magnets, which can be flexibly designed as a hollow mechanical structure. Force analysis reveals the effectiveness of magnetic actuation. Based on this, a movable magnetic field actuation system supplied by a robot arm is presented by fixing a permanent magnet as the end-effector for wirelessly navigating the millirobot in a long-trip 3D vascular model. Three-dimensional electromagnetic coils enable the achievement of more precise local motion control. In addition, with multimodal movements at a space of 0.5–0.7 mm, liquid sampling and cargo delivery of 300–600 µL volume were accomplished under the control of a magnet moved by hand. The output force of 5–20 mN was achieved by both single and multiple MHCMMs, indicating their outstanding potential for complex operations in a confined environment. In future work, we will try to integrate more powerful components (such as sensors) into the microrobots and provide reconfigurable control methods for multiple robots dedicated to various applications.

Author Contributions: Conceptualization, Y.C., Z.X. and Q.X.; methodology, Y.C., Z.X. and Q.X.; software, Y.C. and Z.X.; validation, Y.C. and Z.X.; formal analysis, Y.C. and Z.X.; investigation, Y.C. and Z.X.; data curation, Y.C. and Z.X.; writing—original draft preparation, Y.C., Z.X. and Q.X.; resources, Q.X.; writing—review and editing, Y.C., Z.X. and Q.X.; visualization, Y.C. and Z.X.; supervision, Q.X.; project administration, Q.X.; funding acquisition, Q.X. All authors have read and agreed to the published version of the manuscript.

Funding: This work was funded in part by the National Natural Science Foundation of China (File no. 52175556), The Science and Technology Development Fund, Macau SAR (File no. 0022/2019/AKP and 0153/2019/A3), and University of Macau (File no. MYRG2018-00034-FST and MYRG2019-00133-FST).

Data Availability Statement: Not applicable.

Conflicts of Interest: The authors declare no conflict of interest. The founding sponsors had no role in the design of the study; in the collection, analyses, or interpretation of data; in the writing of the manuscript; or in the decision to publish the results.

References

1. Li, M.; Pal, A.; Aghakhani, A.; Pena-Francesch, A.; Sitti, M. Soft actuators for real-world applications. *Nat. Rev. Mater.* **2022**, *7*, 235–249. [CrossRef]
2. Son, D.; Gilbert, H.; Sitti, M. Magnetically actuated soft capsule endoscope for fine-needle biopsy. *Soft Robot.* **2020**, *7*, 10–21. [CrossRef]
3. Nitta, T.; Wang, Y.; Du, Z.; Morishima, K.; Hiratsuka, Y. A printable active network actuator built from an engineered biomolecular motor. *Nat. Mater.* **2021**, *20*, 1149–1155. [CrossRef]

4. Jin, D.; Yuan, K.; Du, X.; Wang, Q.; Wang, S.; Zhang, L. Domino reaction encoded heterogeneous colloidal microswarm with on-demand morphological adaptability. *Adv. Mater.* **2021**, *33*, 2100070. [CrossRef]
5. Akolpoglu, M.B.; Alapan, Y.; Dogan, N.O.; Baltaci, S.F.; Yasa, O.; Aybar Tural, G.; Sitti, M. Magnetically steerable bacterial microrobots moving in 3D biological matrices for stimuli-responsive cargo delivery. *Sci. Adv.* **2022**, *8*, eabo6163. [CrossRef]
6. Cheng, Y.; Li, S.; Liu, J. Abnormal deformation and negative pressure of a hard magnetic disc under the action of a magnet. *Sens. Actuators Phys.* **2021**, *332*, 113065. [CrossRef]
7. Kim, Y.; Yuk, H.; Zhao, R.; Chester, S.A.; Zhao, X. Printing ferromagnetic domains for untethered fast-transforming soft materials. *Nature* **2018**, *558*, 274–279. [CrossRef]
8. Zhang, J.; Ren, Z.; Hu, W.; Soon, R.H.; Yasa, I.C.; Liu, Z.; Sitti, M. Voxelated three-dimensional miniature magnetic soft machines via multimaterial heterogeneous assembly. *Sci. Robot.* **2021**, *6*, eabf0112. [CrossRef]
9. Wu, Z.; Zhang, Y.; Ai, N.; Chen, H.; Ge, W.; Xu, Q. Magnetic Mobile Microrobots for Upstream and Downstream Navigation in Biofluids with Variable Flow Rate. *Adv. Intell. Syst.* **2022**, *4*, 2100266. [CrossRef]
10. Wu, Z.; Zhang, Y.; Chi, Z.; Xu, Q. Design and Development of a New Rotating Electromagnetic Field Generation System for Driving Microrobots. *IEEE Trans. Magn.* **2021**, *58*, 1–8. [CrossRef]
11. Kearney, K.; Hira, R.S.; Riley, R.F.; Kalyanasundaram, A.; Lombardi, W.L. Update on the management of chronic total occlusions in coronary artery disease. *Curr. Atheroscler. Rep.* **2017**, *19*, 1–10. [CrossRef]
12. Song, P.; Rudan, D.; Zhu, Y.; Fowkes, F.J.; Rahimi, K.; Fowkes, F.G.R.; Rudan, I. Global, regional, and national prevalence and risk factors for peripheral artery disease in 2015: An updated systematic review and analysis. *Lancet Glob. Health* **2019**, *7*, e1020–e1030. [CrossRef]
13. Scales, C.D., Jr.; Smith, A.C.; Hanley, J.M.; Saigal, C.S.; Urologic Diseases in America Project. Prevalence of kidney stones in the United States. *Eur. Urol.* **2012**, *62*, 160–165. [CrossRef]
14. Azizi, A.; Tremblay, C.C.; Gagné, K.; Martel, S. Using the fringe field of a clinical MRI scanner enables robotic navigation of tethered instruments in deeper vascular regions. *Sci. Robot.* **2019**, *4*, eaax7342. [CrossRef]
15. Kim, Y.; Parada, G.A.; Liu, S.; Zhao, X. Ferromagnetic soft continuum robots. *Sci. Robot.* **2019**, *4*, eaax7329. [CrossRef]
16. Jeon, S.; Hoshiar, A.K.; Kim, K.; Lee, S.; Kim, E.; Lee, S.; Kim, J.Y.; Nelson, B.J.; Cha, H.J.; Yi, B.J.; et al. A magnetically controlled soft microrobot steering a guidewire in a three-dimensional phantom vascular network. *Soft Robot.* **2019**, *6*, 54–68. [CrossRef]
17. Khalil, I.S.; Tabak, A.F.; Hosney, A.; Mohamed, A.; Klingner, A.; Ghoneima, M.; Sitti, M. Sperm-shaped magnetic microrobots: Fabrication using electrospinning, modeling, and characterization. In Proceedings of the 2016 IEEE International Conference on Robotics and Automation (ICRA), Stockholm, Sweden, 16–21 May 2016; pp. 1939–1944.
18. Park, M.; Le, T.A.; Yoon, J. Offline Programming Guidance for Swarm Steering of Micro-/Nano Magnetic Particles in a Dynamic Multichannel Vascular Model. *IEEE Robot. Autom. Lett.* **2022**, *7*, 3977–3984. [CrossRef]
19. Dai, Y.; Jia, L.; Wang, L.; Sun, H.; Ji, Y.; Wang, C.; Song, L.; Liang, S.; Chen, D.; Feng, Y.; et al. Magnetically Actuated Cell-Robot System: Precise Control, Manipulation, and Multimode Conversion. *Small* **2022**, *18*, 2105414. [CrossRef]
20. Lin, D.; Wang, J.; Jiao, N.; Wang, Z.; Liu, L. A Flexible Magnetically Controlled Continuum Robot Steering in the Enlarged Effective Workspace with Constraints for Retrograde Intrarenal Surgery. *Adv. Intell. Syst.* **2021**, *3*, 2000211. [CrossRef]
21. Kafash Hoshiar, A.; Jeon, S.; Kim, K.; Lee, S.; Kim, J.y.; Choi, H. Steering algorithm for a flexible microrobot to enhance guidewire control in a coronary angioplasty application. *Micromachines* **2018**, *9*, 617. [CrossRef]
22. Kim, Y.; Genevriere, E.; Harker, P.; Choe, J.; Balicki, M.; Regenhardt, R.W.; Vranic, J.E.; Dmytriw, A.A.; Patel, A.B.; Zhao, X. Telerobotic neurovascular interventions with magnetic manipulation. *Sci. Robot.* **2022**, *7*, eabg9907. [CrossRef] [PubMed]
23. Wang, L.; Kim, Y.; Guo, C.F.; Zhao, X. Hard-magnetic elastica. *J. Mech. Phys. Solids* **2020**, *142*, 104045. [CrossRef]
24. Craik, D.J. *Magnetism: Principles and Applications*; John Wiley & Sons, Inc.: Hoboken, NJ, USA, 2003.
25. Agashe, J.S.; Arnold, D.P. A study of scaling and geometry effects on the forces between cuboidal and cylindrical magnets using analytical force solutions. *J. Phys. Appl. Phys.* **2008**, *41*, 105001. [CrossRef]
26. Di Natali, C.; Beccani, M.; Valdastri, P. Real-time pose detection for magnetic medical devices. *IEEE Trans. Magn.* **2013**, *49*, 3524–3527. [CrossRef]
27. Geiger, M. *Fundamentals of Vascular Biology*; Springer: Cham, Switzerland, 2019.
28. Xu, C.; Yang, Z.; Tan, S.W.K.; Li, J.; Lum, G.Z. Magnetic Miniature Actuators with Six-Degrees-of-Freedom Multimodal Soft-Bodied Locomotion. *Adv. Intell. Syst.* **2022**, *4*, 2100259. [CrossRef]
29. Wu, Y.; Dong, X.; Kim, J.K.; Wang, C.; Sitti, M. Wireless soft millirobots for climbing three-dimensional surfaces in confined spaces. *Sci. Adv.* **2022**, *8*, eabn3431. [CrossRef]